

Near-field ultrasound tomography

Serge Mensah^{a)} and Emilie Franceschini

CNRS-Laboratoire de Mécanique et d'Acoustique, 31 chemin Joseph Aiguier, 13402 Marseille, Cedex 20, France

(Received 6 March 2006; revised 22 December 2006; accepted 2 January 2006)

In this paper, a near-field tomographic solution is introduced to solve the imaging problem of fluid objects assumed to be weakly heterogeneous (Born approximation) and excited by spherical waves. The solution to the forward problem is based on the Huygens-Fresnel principle which describes the scattered field as the result of the interference scheme of all the secondary spherical waves. From the derivation of the scattered field, a new Fourier transform that has been called the elliptical Fourier transform is defined: It differs from the standard Fourier transform in that instead of a plane wave decomposition, a harmonic ellipsoidal wave decomposition is obtained. Based on this spectral analysis, a near-field Radon transform is designed that complements the “far-field tools” published in diffraction tomography literature. Then, assuming that the measuring distance is greater than one wavelength, the feasibility of reconstructing either the impedance or the velocity maps of an acoustical (perfect fluid) model is demonstrated. Numerical simulations were performed which confirmed the validity of the theory presented here; a theory which has many potential applications in future wave theory research. © 2007 Acoustical Society of America. [DOI: 10.1121/1.2436637]

PACS number(s): 43.35.Wa, 43.80.Ev, 43.80.Vj [TDM]

Pages: 1423–1433

I. INTRODUCTION

The use of wide-band information is becoming a common goal for most research teams working on the ultrasonic imaging of weak-scattering media, since it is known to improve point and contrast resolutions, both of which are important criteria for medical applications. Developing quantitative reconstruction procedures is the ultimate goal, so as to improve the specificity of the system as well as performing automatic tissue characterization. Finally, in order to obtain an efficient reconstruction procedure it is important to take into account the true nature of the wave (cylindrical or spherical waves; transducer directivity), which is generally expressed in terms of near-field conditions. So far, there exist very few approaches which meet all the above-mentioned criteria simultaneously. In his pioneering studies, Norton^{1,2} introduced the near-field concept, which makes it possible to deal with spherical waves transmitted around the whole organ as the punctual broadband transducer moves along a circular path. The resulting projections obtained were found to result from surface integration of the reflectivity over the spherical wave fronts. However, the fundamental hypothesis was based on a circular (or spherical) harmonic decomposition of the object, which makes it necessary to use Hankel transforms. These transforms are numerically very unstable, and further approximations are therefore generally required for practical implementation. The second limitation of this pioneering work is the fact that it involves a single transducer acting as both a transmitter and a receiver in the pure reflection mode. Furthermore, diffraction tomography methods have been implemented either with a number of discrete frequencies^{3–6} or with multiple frequencies in order to enhance the image resolution.⁷ Also, with quantitatively accu-

rate reconstruction techniques⁸ the imaging of object of higher contrast and bigger size than permitted by diffraction tomography (Born approximation) becomes possible. However, these linear and nonlinear solutions of the inverse problem have the great disadvantage of requiring a considerable amount of computational resources, especially in the typical case of quantitative imaging, where many frequencies and/or enhanced Green's operator are used to achieve a sufficiently high imaging quality to compete with the diagnostic systems available at present. In the dual space, several researchers^{9–11} have developed direct time-domain scattering methods that overcome most of the limitations inherent in frequency-domain techniques. These methods were designed to obtain quantitative information by performing bistatic or multistatic measurements and attempting to work in the near-field zone. However, the plane wave assumption on which these methods were based is generally not compatible with the way in which present-day scanners function. Recently, some interesting time-domain reconstructions were carried out in the field of thermoacoustic tomography^{12,13} with a view to reconstructing the relative absorption coefficient of biological tissues based on cylindrical or spherical measurement. The prerequisite that the near-field distance must be much greater than the thermoacoustic signals simplifies the exact formulas, and makes it possible to obtain backprojections and weighted time-domain summations over cylindrical or spherical surfaces. Approaches of this kind implicitly make it necessary to invert a generalized (circular) Radon transform.¹⁴ However, here again, no multistatic configurations have so far been used in studies of this kind, since the ultrasound channels operate in a passive mode in these microwave-induced imaging systems.

Lastly, several researchers were interested at an early stage in quantitative reconstruction, and attempted to use the scattering directivity pattern of any acoustical param-

^{a)}Electronic mail: mensah@lma.cnrs-mrs.fr

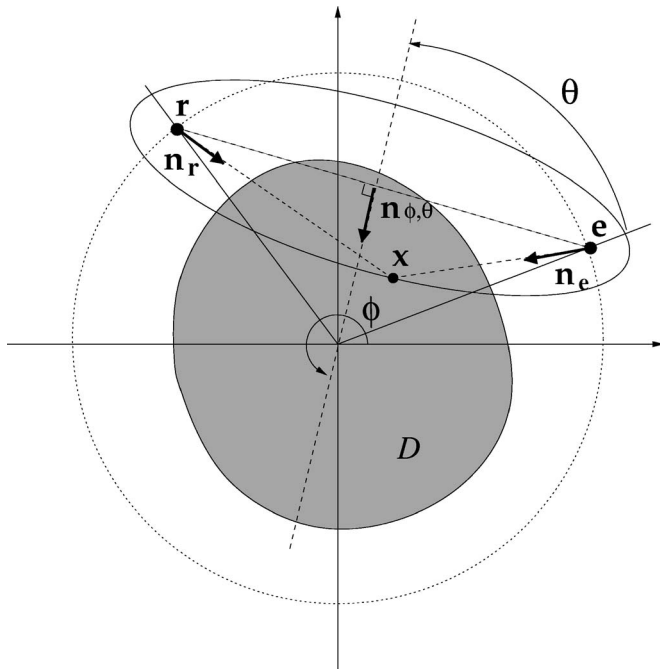


FIG. 1. Scattering acquisition configuration. In active ultrasonic tomography, a transducer \mathbf{e} (which size is smaller than half a wavelength) transmits a spherical wave which is scattered and recorded by a receiver \mathbf{r} placed on the same spherical surface closely surrounding the organ (i.e., the breast).

eters (attenuation and sound speed,¹⁵ density and compressibility,^{16–18} or impedance and sound speed^{19–21}) for this purpose. In addition to these investigations, it is proposed to extend the scope of the research to include near-field conditions (using spherical waves), with broadband signals, the scattering analysis derived using plane wave decomposition methods. Depending on whether the transmission or the reflection mode is involved, this will enable us to separate the respective effects of tissue parameter distributions on the scattering processes. From this analysis, which is valid provided that the observation distance is greater than the wavelength, a two-dimensional (2D) reconstruction scheme was developed, providing an estimate of either impedance or sound speed distributions. The ideal propagative medium is assumed to effect no absorption and to have only weak scattering characteristics. The present reconstruction technique is a near-field extension of the inverse Radon transform: this solution of the linearized scattered inverse problem exploits an optimal fast Fourier transform algorithm.

II. DEFINITION OF THE ELLIPTICAL FOURIER TRANSFORMS

Let us define the compact domain \mathcal{D} of \mathbb{R}^N $N=2, 3$, corresponding to the organ to be imaged and the acquisition sphere (or circle, in the 2D case) \mathcal{S} surrounding the compact domain \mathcal{D} . The acquisition sphere radius \mathcal{R} is such that $\forall x \in \mathcal{D}, \|x\| < \mathcal{R}$. A transducer located in \mathbf{e} , $\mathbf{e} \in \mathcal{S}$, transmits a spherical wave with an angular frequency ω . The field scattered by the medium is recorded in \mathbf{r} , $\mathbf{r} \in \mathcal{S}$.

We take $\mathbf{n}_{\phi, \theta}$ to denote the unit vector of the mediatrix in the incident direction specified by the angles (Fig. 1):

$$\phi = \pi + \frac{1}{2}(\text{angle}(\mathbf{e}) + \text{angle}(\mathbf{r})) \quad \text{the incident angle,}$$

$\theta = \frac{1}{2}|\text{angle}(\mathbf{e}) - \text{angle}(\mathbf{r})|$ the configuration angle in the plane (\mathbf{e}, \mathbf{r}) .

The elliptical wave vector $\mathbf{K} = k\mathbf{n}_{\phi, \theta}$ is then defined. The elliptical scalar product defined for a fixed configuration (\mathbf{e}, \mathbf{r}) or equivalently (ϕ, θ) is introduced:

$$\mathbf{K} \odot \mathbf{x} = k\mathbf{n}_{\phi, \theta} \odot \mathbf{x} \triangleq -k(\|\mathbf{x} - \mathbf{e}_{\mathbf{K}}\| + \|\mathbf{x} - \mathbf{r}_{\mathbf{K}}\|), \quad (1)$$

where $k = \omega/c_0$ is the wave number of the illuminating wave having the sound speed c_0 in the host medium.

Note 1: The negative value of the elliptical scalar product results here from the fact that the wave is propagating toward the origin, and is opposed to the outgoing orientation of the \mathbf{x} axis.

Note 2: According to the definition of an ellipse (ellipsoid), the scalar product verifies: $|\mathbf{K} \odot \mathbf{x}| > k\|\mathbf{r}_{\mathbf{K}} - \mathbf{e}_{\mathbf{K}}\|$ or $\theta < \pi$. Thus, pure transmission measurement appears as a limiting case that can be approximated with any arbitrary precision.

Let $f(\mathbf{x})$ be a well-behaved function defined over \mathcal{D} and null elsewhere. The *elliptical Fourier transform* $\mathcal{F}_{\mathcal{E}}$ is defined by

$$\mathcal{F}_{\mathcal{E}}(f(\mathbf{x})) = \check{f}(\mathbf{K}) = \int f(\mathbf{x}) \frac{e^{-i\mathbf{K} \odot \mathbf{x}}}{[\mathbf{x}]_{\mathbf{K}}} d\mathbf{x} = \int f(\mathbf{x}) \varepsilon^{-i\mathbf{K} \odot \mathbf{x}} d\mathbf{x}. \quad (2)$$

In the last integral, the harmonic decomposition function

$$\varepsilon^{-i\mathbf{K} \odot \mathbf{x}} = \frac{e^{-i\mathbf{K} \odot \mathbf{x}}}{[\mathbf{x}]_{\mathbf{K}}} \quad (3)$$

corresponds to the ellipsoidal harmonic function reduced by the distance $[\mathbf{x}]_{\mathbf{K}}$:

$$[\mathbf{x}]_{\mathbf{K}} = 16\pi^2 \|\mathbf{x} - \mathbf{e}_{\mathbf{K}}\| \cdot \|\mathbf{x} - \mathbf{r}_{\mathbf{K}}\|. \quad (4)$$

The *inverse Elliptical Fourier transform* is then defined as follows:

$$\mathcal{F}_{\mathcal{E}}^{-1}(\check{f}(\mathbf{K})) = f(\mathbf{x}) = \frac{1}{(2\pi)^N} \int \check{f}(\mathbf{K}) [\mathbf{x}]_{\mathbf{K}} e^{i\mathbf{K} \odot \mathbf{x}} d\mathbf{K}, \quad (5)$$

and is written

$$f(\mathbf{x}) = \frac{1}{(2\pi)^N} \int \check{f}(\mathbf{K}) \varepsilon^{i\mathbf{K} \odot \mathbf{x}} d\mathbf{K}. \quad (6)$$

Indeed,

$$\begin{aligned} \mathcal{F}_{\mathcal{E}}^{-1}(\check{f}(\mathbf{K})) &= \frac{1}{(2\pi)^N} \int \check{f}(\mathbf{K}) \varepsilon^{i\mathbf{K} \odot \mathbf{x}} d\mathbf{K} \\ &= \frac{1}{(2\pi)^N} \int \left(\int f(\mathbf{x}') \varepsilon^{-i\mathbf{K} \odot \mathbf{x}'} d\mathbf{x}' \right) \varepsilon^{i\mathbf{K} \odot \mathbf{x}} d\mathbf{K} \\ &= \int f(\mathbf{x}') \frac{1}{(2\pi)^N} \int \varepsilon^{i\mathbf{K} \odot (\mathbf{x} \ominus \mathbf{x}')} d\mathbf{K} d\mathbf{x}', \end{aligned} \quad (7)$$

where we note $\mathbf{K} \odot (\mathbf{x}' \ominus \mathbf{x}) = \mathbf{K} \odot \mathbf{x}' - \mathbf{K} \odot \mathbf{x}$, since the elliptical scalar product “ \odot ” is not distributive. The last integral is the Dirac distribution (Appendix A 1):

$$\frac{1}{(2\pi)^N} \int e^{i\mathbf{K}\odot(\mathbf{x}\oplus\mathbf{x}')} d\mathbf{K} = \frac{1}{(2\pi)^N} \int \frac{[\mathbf{x}]_{\mathbf{K}}}{[\mathbf{x}']_{\mathbf{K}}} e^{i\mathbf{K}\odot(\mathbf{x}\oplus\mathbf{x}')} d\mathbf{K} = \delta(\mathbf{x} - \mathbf{x}') \quad (8)$$

then, in the sense of distributions:

$$\mathcal{F}_{\varepsilon}^{-1}(\check{f}(\mathbf{K})) = \int f(\mathbf{x}') \delta(\mathbf{x} - \mathbf{x}') d\mathbf{x}' = f(\mathbf{x}). \quad (9)$$

The elliptical Fourier transform is an extension of the classical Fourier transform applied to near-field diffraction measurement.

III. FORWARD PROBLEM

We neglect the absorption-dispersion phenomena in order to concentrate on the diffusion resulting from the inhomogeneities. For practical applications of these results, a time gain compensation, TGC, should possibly be used. The inhomogeneous media are described in terms of their density ρ and velocity c distributions. The acoustic pressure p is governed by the wave equation:

$$-\frac{1}{c^2} \frac{\partial^2 p}{\partial t^2} + \rho \nabla \left(\frac{1}{\rho} \nabla p \right) = 0. \quad (10)$$

Let ρ_0, c_0 be the acoustic characteristics of the surrounding medium. The propagation equation can be written as follows:

$$-\frac{1}{c_0^2} \frac{\partial^2 p}{\partial t^2} + \Delta p = \left(\frac{1}{c^2} - \frac{1}{c_0^2} \right) \frac{\partial^2 p}{\partial t^2} + \frac{\nabla \rho}{\rho} \nabla p. \quad (11)$$

We introduce the parameters $2\alpha = (c^2 - c_0^2)/c^2$ and $\xi = \text{Log}(z/z_0)$ corresponding to the quadratic fluctuations of velocity c and to the logarithmic variations of impedance $z = \rho c$, respectively. In view of the development:

$$\frac{\nabla \rho}{\rho} = \nabla \left(\text{Log} \frac{z}{z_0} \right) + \frac{1}{2} \nabla (\text{Log}(1 - 2\alpha)), \quad (12)$$

and the fact that the biological tissues are weakly inhomogeneous media ($\alpha \sim \xi \sim 10^{-2}$), we obtain, at order one in α , the following impedance-velocity propagation equation:²¹

$$-\frac{1}{c_0^2} \frac{\partial^2 p}{\partial t^2} + \Delta p = -\frac{2\alpha}{c_0^2} \frac{\partial^2 p}{\partial t^2} - \nabla \alpha \nabla p + \nabla \xi \nabla p. \quad (13)$$

The medium is excited with a spherical wave having angular frequency ω , the emitter being located in \mathbf{e} :

$$P_i(\mathbf{x}, \mathbf{e}, \omega) = \frac{e^{ik\|\mathbf{x}-\mathbf{e}\|}}{4\pi\|\mathbf{x}-\mathbf{e}\|}. \quad (14)$$

The solution of Eq. (13) is $p = P e^{-i\omega t}$. P is the solution of the Helmholtz equation which can be written in its integral form:

$$P(\mathbf{r}, \mathbf{e}, \omega) = P_i(\mathbf{r}, \mathbf{e}, \omega) + \int_{\mathcal{D}} G(\mathbf{r}, \mathbf{x}, \omega) [2k^2 \alpha(\mathbf{x}) P(\mathbf{x}, \mathbf{e}, \omega) - \nabla \alpha(\mathbf{x}) \cdot \nabla P(\mathbf{x}, \mathbf{e}, \omega) + \nabla \xi(\mathbf{x}) \cdot \nabla P(\mathbf{x}, \mathbf{e}, \omega)] d\mathbf{x}, \quad (15)$$

where the integration volume \mathcal{D} corresponds to the compact

support of α and ξ , and G is the free space Green function; the scattered field is measured in \mathbf{r} :

$$G(\mathbf{r}, \mathbf{x}, \omega) = -\frac{e^{ik\|\mathbf{r}-\mathbf{x}\|}}{4\pi\|\mathbf{r}-\mathbf{x}\|}. \quad (16)$$

Throughout this paper, it is assumed that the acoustical parameters are described by ‘‘well-behaved’’ functions defined over \mathcal{D} and null elsewhere. This means in particular that they have a finite number of discontinuities and turning points (maxima and minima), between which they are monotonic and continuous. Eventually, it also means that they may become infinite, provided that $\int f(\mathbf{x}) d\mathbf{x}$ converges absolutely. Furthermore, we assume that the scattering is sufficiently weak to be able to linearize the inverse problem (using the Born approximation) so that the scattered field P_d becomes

$$P_d = \int G\{2k^2 \alpha P_i - \nabla \alpha \nabla P_i + \nabla \xi \nabla P_i\} d\mathbf{x}. \quad (17)$$

Differentiating P_i yields:

$$\nabla P_i(\mathbf{x}, \mathbf{e}, \omega) = \left(ik - \frac{1}{\|\mathbf{x}-\mathbf{e}\|} \right) \nabla (\|\mathbf{x}-\mathbf{e}\|) \frac{e^{ik\|\mathbf{x}-\mathbf{e}\|}}{4\pi\|\mathbf{x}-\mathbf{e}\|}. \quad (18)$$

In Eq. (18), $1/\|\mathbf{x}-\mathbf{e}\|$ is negligible in comparison with ik . Indeed, in soft tissues, $c_0 \approx 1540 \text{ m s}^{-1}$; and in the near-field zone of interest, $\|\mathbf{x}-\mathbf{e}\| \approx 10^{-2} \text{ m}$. The angular frequency components of the transmitted pulse (based on current echographs) are generally larger than $\omega_{\text{ref}} = 2\pi \cdot 2.5 \times 10^6 \text{ rad s}^{-1}$; thus $k\|\mathbf{x}-\mathbf{e}\| \approx 10^2 \text{ rad}$. The observation distance is greater than the wavelength.

We define \mathbf{n}_e (respectively, \mathbf{n}_r) as the unit vector along the emitter (respectively, receiver) -voxel line that we call the $\mathbf{e}-\mathbf{x}$ axis (respectively, the $\mathbf{x}-\mathbf{r}$ axis): $\mathbf{n}_e = \nabla(\|\mathbf{x}-\mathbf{e}\|)$. This gives

$$\nabla P_i(\mathbf{x}, \mathbf{e}, \omega) \simeq ik \mathbf{n}_e \frac{e^{ik\|\mathbf{x}-\mathbf{e}\|}}{4\pi\|\mathbf{x}-\mathbf{e}\|}, \quad (19)$$

and Eq. (17) becomes

$$P_d = - \int \frac{e^{ik(\|\mathbf{r}-\mathbf{x}\| + \|\mathbf{x}-\mathbf{e}\|)}}{16\pi^2 \|\mathbf{r}-\mathbf{x}\| \|\mathbf{x}-\mathbf{e}\|} \times \{2k^2 \alpha - ik \mathbf{n}_e \cdot [\nabla \alpha - \nabla \xi]\} d\mathbf{x}. \quad (20)$$

According to the definition of the elliptical Fourier transform in Sec. II, the scattered field Eq. (20) is

$$P_d = - \int_{\mathcal{D}} \varepsilon^{-i\mathbf{K}\odot\mathbf{x}} \{2k^2 \alpha - ik \mathbf{n}_e \cdot [\nabla \alpha - \nabla \xi]\} d\mathbf{x}, \quad (21)$$

and P_d then reduces to

$$P_d(\mathbf{K}) = - \mathcal{F}_{\varepsilon} \{2k^2 \alpha - ik \mathbf{n}_e \cdot [\nabla \alpha - \nabla \xi]\}(\mathbf{K})|_{\mathbf{K}=k\mathbf{n}_{\phi, \theta}}. \quad (22)$$

When taking $\check{\mathcal{K}}_{\mathbf{K}} = \mathcal{F}_{\varepsilon}[-ik(1 + \mathbf{n}_{\mathbf{e}_{\mathbf{K}}} \cdot \mathbf{n}_{\mathbf{r}_{\mathbf{K}}})]$, the derivation rule introduced in Appendix A 2 yields

$$P_d(\mathbf{K}) \simeq - \{2k^2 \check{\alpha}(\mathbf{K}) - ik[\check{\mathcal{K}}_{\mathbf{K}} \circledast (\check{\alpha} - \check{\xi})](\mathbf{K})\}, \quad (23)$$

where ‘‘ \circledast ’’ is the elliptical convolution (cf Appendix A 2). We note

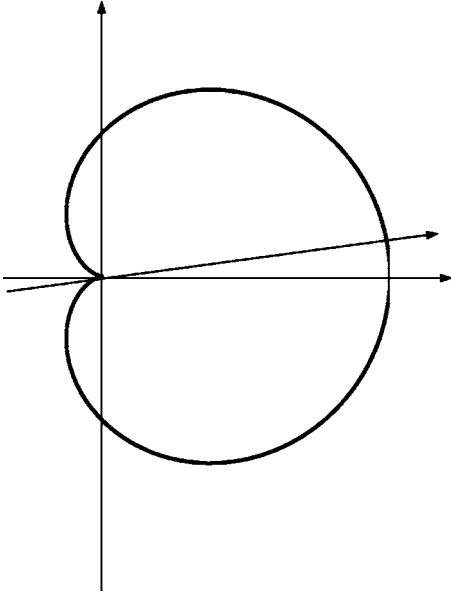


FIG. 2. Directivity diagrams of α : The velocity effects predominate in the transmission mode.

$$P_d(\mathbf{e}, \mathbf{r}, \omega) = -h(\mathbf{e}, \mathbf{r}, \omega), \quad (24)$$

then

$$h(\mathbf{e}, \mathbf{r}, \omega) = k^2 [\mathcal{F}_\mathcal{E}(1 - \mathbf{n}_e \cdot \mathbf{n}_r) \otimes \check{\alpha} + \mathcal{F}_\mathcal{E}(1 + \mathbf{n}_e \cdot \mathbf{n}_r) \otimes \check{\xi}](\mathbf{K}), \quad (25)$$

where $\check{\alpha}(\mathbf{K})$ and $\check{\xi}(\mathbf{K})$ are the elliptical Fourier transforms of the functions $\alpha(\mathbf{x})$ and $\xi(\mathbf{x})$:

$$\begin{aligned} \check{\alpha}(\mathbf{K}) &= \int \alpha(\mathbf{x}) \varepsilon^{-i\mathbf{K} \odot \mathbf{x}} d\mathbf{x}, \\ \check{\xi}(\mathbf{K}) &= \int \xi(\mathbf{x}) \varepsilon^{-i\mathbf{K} \odot \mathbf{x}} d\mathbf{x}. \end{aligned} \quad (26)$$

h represents the elliptical spatial transfer function of the medium in the case of a specific configuration defined by \mathbf{e} and \mathbf{r} . This configuration involves two parameters offering opposite local directivity diagrams: the velocity predominates in the transmission mode (Fig. 2); whereas the impedance predominates in the reflection mode (Fig. 3). This composite object results in a summation of the elementary contributions integrated over the whole object volume, weighted by their local directivity indexes. When $\mathbf{n}_e = \mathbf{n}_r$, i.e., in the pure reflection mode,

$$h(\mathbf{e}, \mathbf{r}, \omega) = 2k^2 \check{\xi}(\mathbf{K})|_{\mathbf{K}=k\mathbf{n}_{\phi,0}}. \quad (27)$$

When $\mathbf{n}_e \simeq -\mathbf{n}_r$, i.e., in the pure transmission mode,

$$h(\mathbf{e}, \mathbf{r}, \omega) = 2k^2 \check{\alpha}(\mathbf{K})|_{\mathbf{K}=k\mathbf{n}_{\phi,\pi}}. \quad (28)$$

At this stage, we have derived a practical means of separating the respective contributions of the impedance fluctuations and those of the sound speed fluctuations to the near-field data. The simplest way of effecting this separation is to work in either the transmission or the reflection mode.

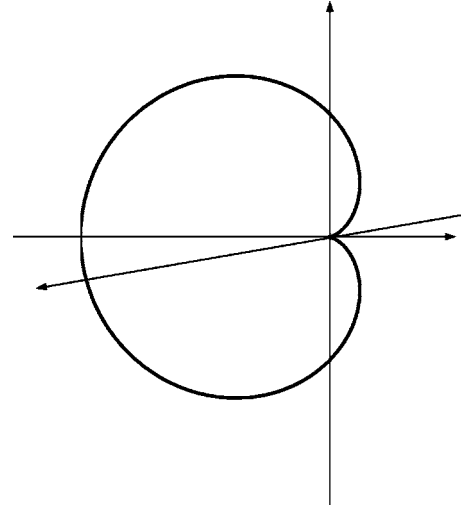


FIG. 3. Directivity diagrams of ξ : The impedance fluctuations account mainly for the scattering in the reflection mode.

IV. INVERSE PROBLEM

By applying the inverse elliptical Fourier transform to the elliptical spectra, we are able to reconstruct either the impedance or the sound speed map. For this purpose, the acquisition procedure used consists of filling in the respective elliptical Fourier domains with the highest sampling densities by performing both a spatial scan and a frequency sweep using broadband signals. However, in practice, since the ultrasonic transducers have a finite bandwidth, one can expect to be able to reconstruct only a bandpass (respectively, low-pass) filtered version of the impedance (respectively, sound speed). Besides, rather than using multidimensional inverse elliptical Fourier transforms to retrieve the object from diffraction measures, it is better to use a reconstruction procedure based on classical one-dimensional (1D) Fourier transforms, with which so many signal processing devices have been optimized. We therefore defined a near-field extension of the Radon transform $\mathcal{R}_\mathcal{E}$, thus restricting our derivation to the 2D case.

A. The 2D elliptical Radon transform and the elliptical Fourier projection-slice theorem

Let $f(\mathbf{x})$ be a well-behaved object function defined over the compact domain \mathcal{D} of \mathbb{R}^2 . f represents either the quadratic fluctuation of the velocity α or the logarithmic variation of the impedance ξ . We may define the elliptical Radon transform by

$$\begin{aligned} [\mathcal{R}_\mathcal{E}f](s, \phi, \theta) &= \int f(\mathbf{x}) \frac{\delta(s - \|\mathbf{x} - \mathbf{e}\| + \|\mathbf{r} - \mathbf{x}\|)}{[\mathbf{x}]_{\phi, \theta}} d\mathbf{x} \\ &= \int f(\mathbf{x}) d\sigma_{\phi, \theta}(\mathbf{x}), \end{aligned} \quad (29)$$

where $d\sigma_{\phi, \theta}(\mathbf{x})$ is the ellipse $s = \|\mathbf{x} - \mathbf{e}\| + \|\mathbf{r} - \mathbf{x}\|$ of foci $(\mathbf{e}, \mathbf{r}) \in \mathcal{S}^2$ (weighted by $[\mathbf{x}]_{\phi, \theta}$). It is clear, however, that this mapping is overdetermined, since the dimension of triplet (s, ϕ, θ) is $N+1$, while the function f depends on $N=2$ variables only. Thus, from the outset, we fix the configuration

angle $\theta = \theta_0$ at a constant value, we therefore drop this subscript from the following expressions.

The acquisition configuration allows us to obtain one of the 1D projections, $p_\phi(s)$, under the incidence ϕ with $\phi \in [0, \pi]$ that belongs to the elliptical Radon transform of the object function f :

$$[\mathcal{R}_{\mathcal{E}f}](s, \phi) = \{p_\phi(s), s \in \mathbb{R}, 0 \leq \phi \leq \pi\}, \quad (30)$$

$$[\mathcal{R}_{\mathcal{E}f}](s, \phi)|_{\phi \text{ fixed}} = p_\phi(s). \quad (31)$$

The standard Fourier transform F of a projection $p_\phi(s)$, $\hat{p}_\phi(S)$, is written:

$$\hat{p}_\phi(S) = (F[p_\phi])(S) = \int_{-\infty}^{\infty} p_\phi(s) e^{-iSs} ds. \quad (32)$$

Substituting $p_\phi(s)$ by its expression [Eq. (29)], implies that:

$$\begin{aligned} \hat{p}_\phi(S) &= \int \int f(\mathbf{x}) \frac{\delta(s - \mathbf{n}_\phi \odot \mathbf{x})}{[\mathbf{x}]_\phi} e^{-iSs} d\mathbf{x} ds \\ &= \int f(\mathbf{x}) \int \frac{\delta(s - \mathbf{n}_\phi \odot \mathbf{x})}{[\mathbf{x}]_\phi} e^{-iS \mathbf{n}_\phi \odot \mathbf{x}} ds d\mathbf{x}. \end{aligned} \quad (33)$$

We denote $S \mathbf{n}_\phi = \mathbf{S}_\phi$, then

$$\hat{p}_\phi(S) = \int f(\mathbf{x}) \varepsilon^{-iS \phi \odot \mathbf{x}} d\mathbf{x} = \check{f}(S, \phi)|_{\phi \text{ fixed}} = \mathcal{F}_{\mathcal{E}|\phi}[f](S). \quad (34)$$

The standard Fourier transform of a projection is therefore a slice of the 2D elliptical Fourier transform of the object function. This result can be said to be a near-field extension of the Fourier projection-slice theorem.

B. Inversion procedure

The inverse of the elliptical Radon transform is derived in Appendix B. Here, the focus is on the inversion procedure: Let us take a two-dimensional function f , and apply the direct and inverse elliptical Fourier transforms and use polar coordinates to obtain:

$$\begin{aligned} f(\mathbf{x}) &= \frac{1}{(2\pi)^2} \int_{-\infty}^{\infty} \check{f}(\mathbf{K}) e^{i\mathbf{K} \odot \mathbf{x}} [\mathbf{x}]_{\mathbf{K}} d\mathbf{K} \\ &= \frac{1}{(2\pi)^2} \int_0^{2\pi} \int_0^{\infty} \mathcal{F}_{\mathcal{E}}[f](S, \phi) e^{iS \phi \odot \mathbf{x}} [\mathbf{x}]_\phi S dS d\phi \\ &= \frac{1}{(2\pi)^2} \int_0^{\pi} \int_{-\infty}^{\infty} \mathcal{F}_{\mathcal{E}|\phi}[f](S) |S| e^{iS \phi \odot \mathbf{x}} [\mathbf{x}]_\phi dS d\phi \\ &= \frac{1}{(2\pi)^2} \int_0^{\pi} \int_{-\infty}^{\infty} \hat{p}_\phi(S) |S| e^{iS \phi \odot \mathbf{x}} [\mathbf{x}]_\phi dS d\phi. \end{aligned} \quad (35)$$

The inversion scheme is as follows:

$$f(\mathbf{x}) = \frac{1}{2} \times \frac{1}{\pi} \int_0^{\pi} \Pi_\phi(\mathbf{x}) d\phi \quad (36)$$

is the sum of the Elliptical backprojections $\Pi_\phi(\mathbf{x})$:

$$\begin{aligned} \Pi_\phi(\mathbf{x}) &= \frac{1}{2\pi} \int \hat{p}_\phi(S) |S| e^{iS \phi \odot \mathbf{x}} [\mathbf{x}]_\phi dS \\ &= \frac{[\mathbf{x}]_\phi}{2\pi} \int \int \hat{p}_\phi(S) |S| e^{iSs} \delta(s - \mathbf{n}_\phi \odot \mathbf{x}) dS ds \\ &= [\mathbf{x}]_\phi p_\phi^F(s = \mathbf{n}_\phi \odot \mathbf{x}) \end{aligned} \quad (37)$$

of the filtered projections p_ϕ^F :

$$\begin{aligned} p_\phi^F(s) &= \frac{1}{2\pi} \int_{-\infty}^{\infty} \hat{p}_\phi(S) |S| e^{iSs} dS \\ &= F^{-1}[|S| \hat{p}_\phi(S)] \\ &= F^{-1}[\mathbf{K} |\hat{p}_\phi(\mathbf{K})]. \end{aligned} \quad (38)$$

This inversion algorithm turns out to be quite similar to the classical backprojection of the filtered projection algorithm used so far in computer-assisted tomography; only the nature of the projections differs.

C. Backprojection operator

Consider an arbitrary function $h(s, \phi)$ where $s = \mathbf{n}_\phi \odot \mathbf{x}$. The backprojection operator \mathcal{B} is defined by²²:

$$\mathcal{B}[h(s, \phi)](\mathbf{x}) = \frac{1}{2} \times \frac{1}{\pi} \int_0^{\pi} [\mathbf{x}]_\phi h(\mathbf{n}_\phi \odot \mathbf{x}, \phi) d\phi. \quad (39)$$

It is helpful to introduce the modified projection function f^* as follows:

$$f^*(s, \phi) = F^{-1}[|S| F[\mathcal{R}_{\mathcal{E}f}](S)], \quad (40)$$

the function f is then recovered by backprojection, (cf. Appendix B)

$$f(\mathbf{x}) = \mathcal{B}f^* = \frac{1}{2} \times \frac{1}{\pi} \int_0^{\pi} [\mathbf{x}]_\phi f^*(\mathbf{n}_\phi \odot \mathbf{x}, \phi) d\phi, \quad (41)$$

or

$$f = \mathcal{B} \circ F^{-1} \circ \text{Abs} \circ F \circ \mathcal{R}_{\mathcal{E}} \circ f, \quad (42)$$

where the filter Abs has the response $\text{Abs}(S) = |S|$.

V. NUMERICAL SIMULATIONS

In order to assess the reconstruction procedure presented in Sec. IV, we use a 2D numerical tissue-like phantom giving a scattering response which is computed using a finite element method (FEM). This method, which was developed in Refs. 23 and 24, models the time-domain acoustic wave propagation occurring in fluid media and is based on the discretization of the mixed velocity-pressure formulation of acoustics. One of the advantages of this method is that it requires no physical approximations to be made in the framework of linear acoustics; our method thus automatically accounts for multiple scattering, refraction, and reflection. The space discretization of the problem is based on a mixed finite element method²⁴ and the discretization in time is performed using a second-order-centered finite difference scheme. The simulation grid is surrounded by an absorbing layer (PML) simulating unbounded domains.²⁵

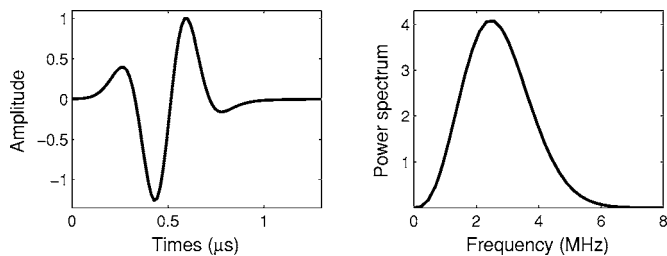


FIG. 4. 2.5 MHz cylindrical wave used in the FEM simulations in the time and frequency domains.

The size of the spatial step in the finite element grid is taken to be one thirtieth of the wavelength. A grid consisting of 1000×1000 pixels ($\Delta x = 0.016$ mm, 1.6 cm \times 1.6 cm) is used here. The ring transducer array is composed of 360 equally spaced transducers (point-like transmitters and receivers, central frequency 2.5 MHz, $\lambda = 0.6$ mm) and has a radius of $R = 7.36$ mm. The diameter of the ring transducer is fixed in order to obtain an acceptable computation time (simulation of the forward problem). This results in an element spacing (pitch) of 0.21λ . In ultrasound research, recent ring transducer systems already use 0.38λ pitch arrays in order to refine the transmitted wave front and to reduce the image reconstruction noise.²⁶ In the simulation, each transducer transmits a short pulse, while the remaining elements act as receivers. The temporal and spectral plots of the transmitted pulses are shown in Fig. 4. The cylindrical academic phantom simulates holes evenly spaced along a spiral immersed in water (Fig. 5). The radii of the holes are $r_1 = r_{1'} = 1.32$ mm, $r_2 = r_{2'} = r_1/2 = 0.66$ mm, $r_3 = r_{3'} = r_1/4 = 0.33$ mm, and $r_4 = r_{4'} = r_1/8 = 0.165$ mm. Each member of a pair of holes having the same radius has either a fixed impedance contrast (and no sound speed contrast, Fig. 6) or a sound speed contrast (and no impedance contrast, Fig. 7). The acoustic properties of the phantom are described in Table I.

Figure 8 shows the impedance tomogram reconstructed with the elliptical backprojection (EBP) procedure when the data were acquired in the pure reflection mode. One can note the image's high-quality contrast and its high resolution: This

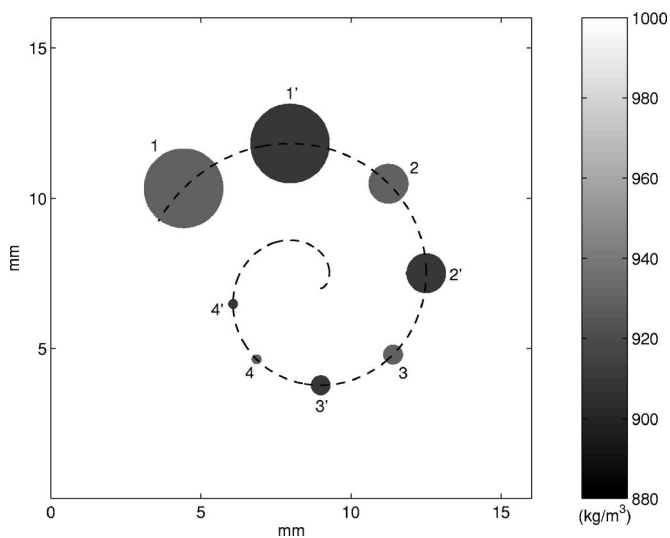


FIG. 5. Density map.

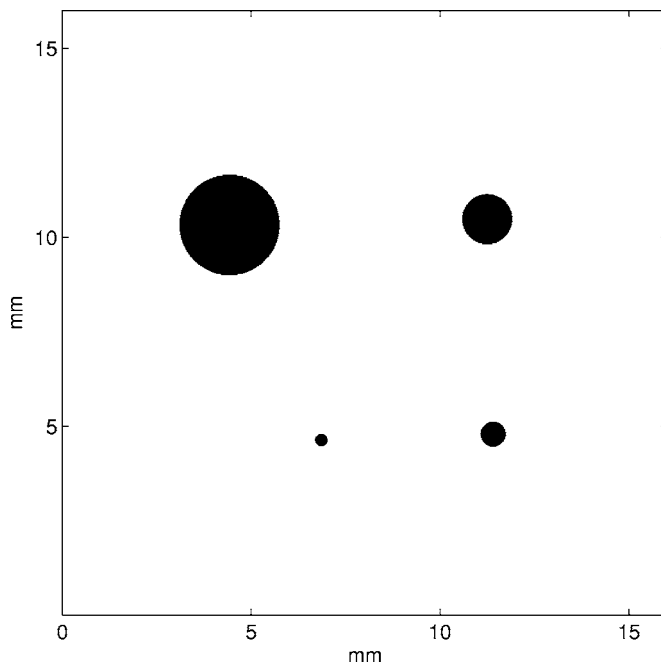


FIG. 6. The numerical phantom of Fig. 5 shows distinct contrast supports (location of the holes) of the acoustical parameters: the impedance map (surrounding medium 1.5 MRa; holes 1.395 MRa).

procedure makes it possible to detect objects of one half the wavelength. Figure 9 illustrates the phantom sound speed reconstructed via the EBP technique in the transmission mode. The time of flight (TOF) between the transmitter and the receiver was estimated using the first zero crossing method. When compared with the impedance reconstructed image, both the contrast and the resolution are poorer because of the low-pass filtering of the projections resulting from the TOF measurements. In the transmission mode, the

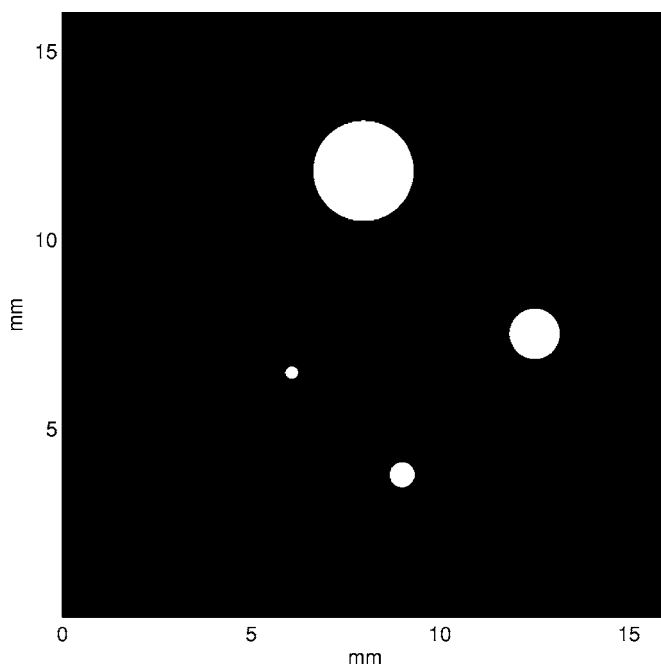


FIG. 7. The numerical phantom of Fig. 5 shows distinct contrast supports (location of the holes) of the acoustical parameters: the sound speed map (surrounding medium 1500 m/s; holes 1650 m/s).

TABLE I. Acoustical properties

Medium	Impedance (MRa)	Sound speed (m/s)	Density (kg/m ³)
Water	1.5	1500	1000
Holes 1, 2, 3,4	1.395	1500	930
Holes 1', 2', 3', 4'	1.5	1650	909.09

EBP procedure makes it possible to detect objects as large as the wavelength and to discriminate defects twice the size of the wavelength. Figure 10 shows the tomogram of the reconstructed objects using projections acquired in the diffraction mode ($\theta=40^\circ$). As the theoretical analysis indicated, one reconstructs a composite object combining the two acoustical parameters (namely impedance and sound speed), each of which is weighted by its own directivity function. Figures 11 and 12 show the poor image quality of the near-field reconstruction obtained when plane waves are transmitted within the medium and when the standard filtered backprojection (FBP) algorithm is used. The scatterers are badly localized: Instead of the radial distance from a point-like transducer, the projected distance from the plane source surface is estimated. With far-field measurements, the distortions are reduced since, locally, the cylindrical waves may be approximated by plane waves.

In conclusion, these numerical simulations confirm that this method makes it possible to separate either of the acoustical parameter contributions from the near-field data. In addition, the directivity functions constitute useful *a priori* information for the optimal processing of near-field scattering data.

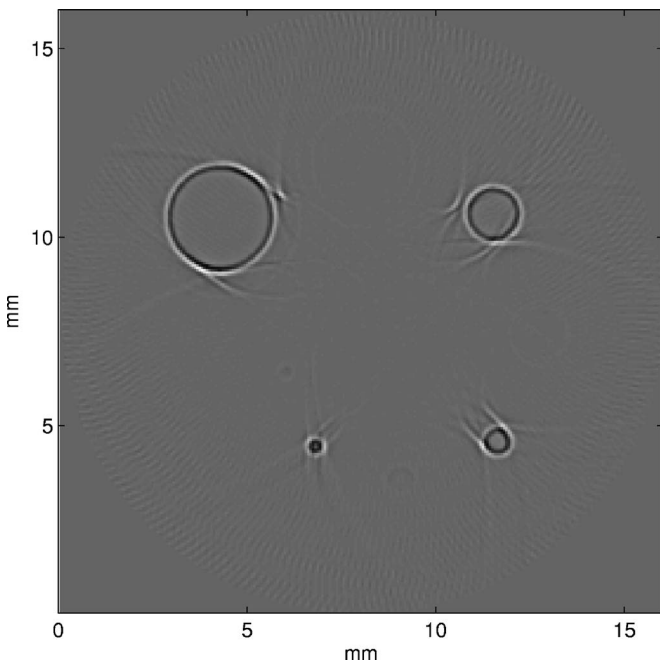


FIG. 8. EBP impedance reconstruction of the numerical phantom of Fig. 5. The acoustical parameters are separated according to the acquisition mode used: here pure reflection.

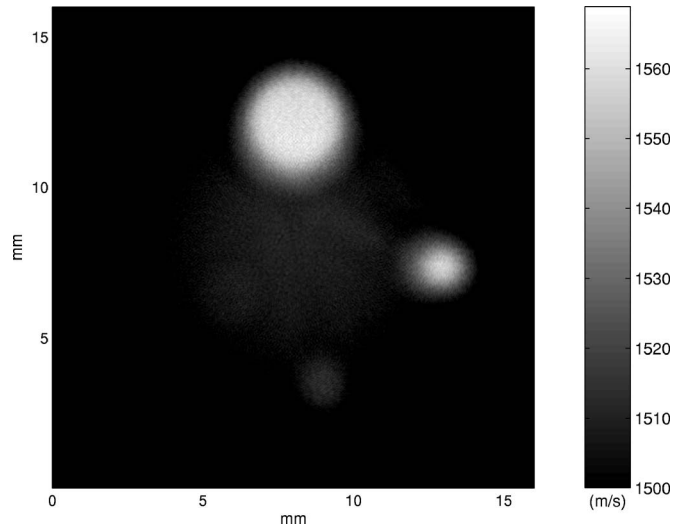


FIG. 9. EBP sound speed reconstruction of the numerical phantom of Fig. 5. The acoustical parameters are separated according to the acquisition mode used: here pure transmission.

VI. CONCLUSION

In quantitative (parametric) imaging and tissue characterization methods, the use of ultrasonic waves requires that the true nature of the waves be taken into consideration. Given the propagating distances generally employed, the shape of the actual wave front transmitted from an active probe element is practically spherical, and plane wave decomposition methods are therefore not optimal.

The derivation of the field scattered by a biological object (specified in terms of density and sound speed maps) shows three-dimensional (3D) ellipsoidal projections (depending on the time) on increasing ellipsoids; the foci of which coincide with the position of the transmitter and re-

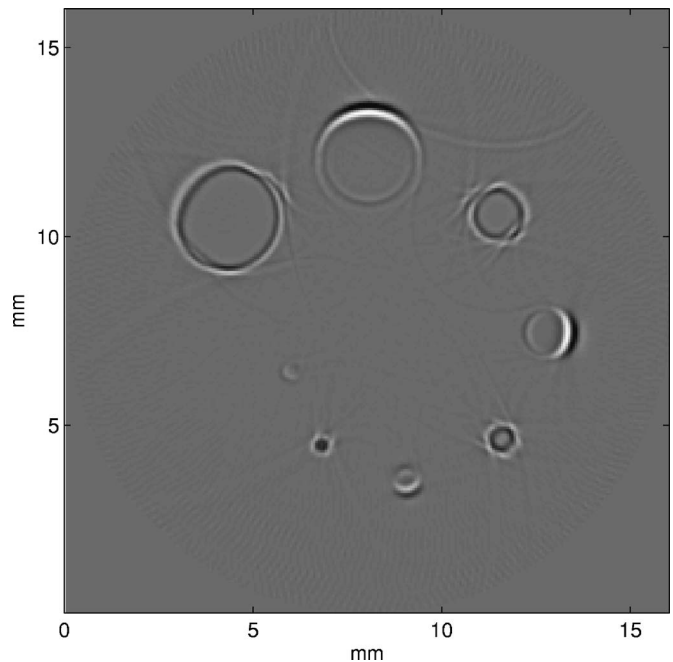


FIG. 10. Composite object reconstructed from diffraction measurements ($\theta=40^\circ$). The acoustical parameter contributions are combined.

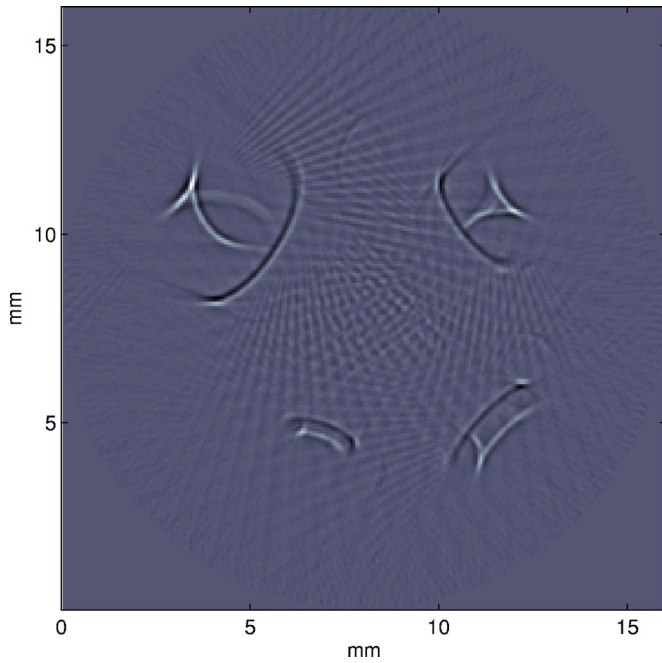


FIG. 11. Impedance reconstruction of the numerical phantom of Fig. 5: plane wave excitation (2.5 MHz central frequency), standard backprojection (FBP) algorithm in pure reflection.

ceiver. The amplitude of these projections is constrained by the fluctuations in impedance and in sound speed.

This ellipsoidal projection problem motivated the search for a harmonic ellipsoidal decomposition of the scattered field in line with the plane wave decomposition performed in Fourier spectral analysis. For this purpose, we defined an elliptical scalar product and an elliptical Fourier transform pair which enable us to model the scattered field spectrum in the form of an elliptical transfer function. This function de-

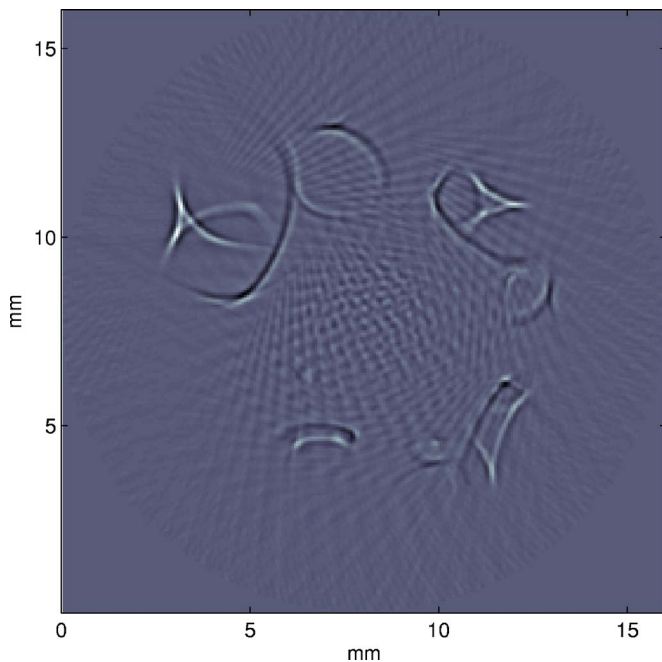


FIG. 12. Composite object reconstructed from diffraction measurements ($\theta=40^\circ$): plane wave excitation (2.5 MHz central frequency), standard backprojection (FBP) algorithm.

pend on the elliptical spectra of impedance and of sound speed, which give opposite local directivity diagrams: Impedance predominates in the reflection mode, whereas velocity predominates in the transmission mode. This makes it possible to reconstruct the impedance or the sound speed maps, depending on the data acquisition procedure used. Each of these parameters can thus be retrieved by applying an inverse 2D elliptical Fourier transform. However, it is better to adopt the optimized 1D fast Fourier transform algorithm used in the inverse elliptical Radon transform introduced here.

Numerical wave propagation simulations and the reconstruction of a tissue-mimicking phantom showing distinct contrast supports (for both impedance and sound speed fluctuations) confirm the validity of the present theory. This near-field scattering theory has many potential applications not only in the field of ultrasound imaging but also in the context of general wave theory.

ACKNOWLEDGMENTS

This study was supported by the City of Marseille, Region Provence-Alpes-Côte d'Azur, Conseil Général 13, CNRS-LMA. The authors would like to thank the Institute for Development and Resources in Intensive Scientific Computing (IDRIS) where the computations were performed. We are grateful to Chrysoula Tsogka (a researcher at CNRS) for placing her propagation code at our disposal.

APPENDIX A: ELLIPTICAL FOURIER TRANSFORMS

1. Dirac distributions

Let us consider the $I_{\mathbf{x}_0}(\mathbf{x})$ following integral of the variable $\mathbf{x} \in \mathcal{D}$ ($\mathcal{D} \subset \mathbb{R}^2$), where the fixed point \mathbf{x}_0 acts as a parameter:

$$I_{\mathbf{x}_0}(\mathbf{x}) = \frac{1}{(2\pi)^2} \int \frac{[\mathbf{x}_0]_{\mathbf{K}}}{[\mathbf{x}]_{\mathbf{K}}} e^{i\mathbf{K} \odot (\mathbf{x}_0 \ominus \mathbf{x})} d\mathbf{K}, \quad (\text{A1})$$

where $\mathbf{K} = k\mathbf{n}_{\phi, \theta}$ is a wave vector of the 2D elliptical Fourier domain, whose configuration angle θ is fixed. Then changing to polar coordinates, one obtains:

$$\begin{aligned} I_{\mathbf{x}_0}(\mathbf{x}) &= \frac{1}{(2\pi)^2} \int_0^{2\pi} \frac{[\mathbf{x}_0]_{\phi}}{[\mathbf{x}]_{\phi}} \int e^{ik\mathbf{n}_{\phi} \odot (\mathbf{x}_0 \ominus \mathbf{x})} k dk d\phi \\ &= \frac{i}{(2\pi)^2} \int_0^{2\pi} \mathbf{m}_{\phi}(\mathbf{x}) \nabla \left(\int e^{ik\mathbf{n}_{\phi} \odot (\mathbf{x}_0 \ominus \mathbf{x})} dk \right) d\phi \\ &= \frac{i}{2\pi} \int_0^{2\pi} \mathbf{m}_{\phi}(\mathbf{x}) \delta'(\mathbf{n}_{\phi} \odot (\mathbf{x}_0 \ominus \mathbf{x})) d\phi, \quad (\text{A2}) \end{aligned}$$

$$\mathbf{m}_{\phi}(\mathbf{x}) = \frac{[\mathbf{x}_0]_{\phi}}{[\mathbf{x}]_{\phi}} \frac{\mathbf{n}_e + \mathbf{n}_r}{\|\mathbf{n}_e + \mathbf{n}_r\|^2}$$

is a differentiable (since $\mathbf{n}_e \neq -\mathbf{n}_r$) vector function and δ' is the first derivative of the Dirac distribution. The last integral may be written using the $\delta_{\mathcal{E}, \phi, \mathbf{x}_0}(\mathbf{x})$ distribution supported on the ellipse of ϕ direction, crossing the points \mathbf{x}_0 and \mathbf{x} , whose foci are on the \mathcal{S} circle:

$$I_{\mathbf{x}_0}(\mathbf{x}) = \frac{i}{2\pi} \int_0^{2\pi} \mathbf{m}_{\phi}(\mathbf{x}) \delta'_{\mathcal{E}, \phi, \mathbf{x}_0}(\mathbf{x}) d\phi. \quad (\text{A3})$$

Thus, $I_{\mathbf{x}_0}(\mathbf{x})$, as a sum of $\delta_{\mathcal{E}, \phi, \mathbf{x}_0}$ distributions as ϕ varies, is a distribution that can be approached by a discrete summation:

$$I_{\mathbf{x}_0}(\mathbf{x}) = \lim_{N \rightarrow \infty} \frac{i}{N} \sum_{n=0}^{N-1} \mathbf{m}_{\phi_n}(\mathbf{x}) \delta'_{\mathcal{E}, \phi_n, \mathbf{x}_0}(\mathbf{x}) \quad \text{with } \phi_n = \frac{2n\pi}{N}. \quad (\text{A4})$$

Let us now consider an arbitrary parameter function g whose support is included in \mathcal{D} . Here, we can distinguish two cases:

(1) $\mathbf{x} \neq \mathbf{x}_0$: then only two ellipses $\delta_{\mathcal{E}, \phi_1, \mathbf{x}_0}(\mathbf{x})$ and $\delta_{\mathcal{E}, \phi_2, \mathbf{x}_0}(\mathbf{x})$ crossing simultaneously \mathbf{x} and \mathbf{x}_0 and whose foci are on \mathcal{S} exist: For instance, in the incident direction defined by \mathbf{x}_0 , $\phi = \phi_0$, let us consider the ellipse crossing \mathbf{x}_0 and let us follow it as ϕ varies (in the positive and in the negative directions) until it also crosses \mathbf{x} . Therefore, since ϕ_1 and ϕ_2 are not necessarily rational numbers:

$$\begin{aligned} \langle I_{\mathbf{x}_0}(\mathbf{x}), g \rangle &\leq \lim_{N \rightarrow \infty} \frac{i}{N} [\mathbf{m}_{\phi_1}(\mathbf{x}) \langle \delta'_{\mathcal{E}, \phi_1, \mathbf{x}_0}(\mathbf{x}), g \rangle + \mathbf{m}_{\phi_2}(\mathbf{x}) \\ &\quad \times \langle \delta'_{\mathcal{E}, \phi_2, \mathbf{x}_0}(\mathbf{x}), g \rangle] = 0. \end{aligned} \quad (\text{A5})$$

The null value is obtained since the two elliptical projections of g' are finite quantities.

(2) $\mathbf{x} = \mathbf{x}_0$ the calculus of $I_{\mathbf{x}_0}(\mathbf{x} = \mathbf{x}_0)$ is straightforward: $I_{\mathbf{x}_0}(\mathbf{x}_0) = \infty$. To sum up:

$$I_{\mathbf{x}_0}(\mathbf{x}) = \delta(\mathbf{x} - \mathbf{x}_0). \quad (\text{A6})$$

The 3D extension of this relation can be made according to a similar derivation:

$$\frac{1}{(2\pi)^N} \int \frac{[\mathbf{x}_0]_{\mathbf{K}}}{[\mathbf{x}]_{\mathbf{K}}} e^{i\mathbf{K} \odot (\mathbf{x}_0 \odot \mathbf{x})} d\mathbf{K} = \delta(\mathbf{x} - \mathbf{x}_0). \quad (\text{A7})$$

This relation enables us to validate the expression of the inverse elliptical transform (5). In addition one can show that

$$\delta(\mathbf{K} - \mathbf{Z}) = \frac{1}{(2\pi)^N} \int \frac{[\mathbf{x}]_{\mathbf{Z}}}{[\mathbf{x}]_{\mathbf{K}}} e^{-i(\mathbf{K} \odot \mathbf{Z}) \odot \mathbf{x}} d\mathbf{x}, \quad (\text{A8})$$

$$\delta(\mathbf{K} - \mathbf{Z} - \mathbf{Y}) = \frac{1}{(2\pi)^{2N}} \int \frac{[\mathbf{x}]_{\mathbf{Z}} [\mathbf{x}]_{\mathbf{Y}}}{[\mathbf{x}]_{\mathbf{K}}} e^{-i(\mathbf{K} \odot \mathbf{Z} \odot \mathbf{Y}) \odot \mathbf{x}} d\mathbf{x}. \quad (\text{A9})$$

2. Derivation rule

Let us calculate the value of the elliptical Fourier transform of the projected gradient (directional derivative), $\mathbf{n}_{e_{\mathbf{K}}} \cdot \nabla g(\mathbf{x})$, of the parameter function g defined over a compact support \mathcal{D} . This derivation is performed at the arbitrary elliptical spectral location $\mathbf{K} = k\mathbf{n}_{\phi, \theta = \theta_0}$:

$$\begin{aligned} \mathcal{F}_{\mathcal{E}}(\mathbf{n}_{e_{\mathbf{K}}} \cdot \nabla g)(\mathbf{K}) &= \int \nabla g(\mathbf{x}) \cdot \mathbf{n}_{e_{\mathbf{K}}}(\mathbf{x}) \varepsilon^{-i\mathbf{K} \odot \mathbf{x}} d\mathbf{x} \\ &= \int \nabla \left(\frac{1}{(2\pi)^N} \int \check{g}(\Gamma) \varepsilon^{i\Gamma \odot \mathbf{x}} d\Gamma \right) \\ &\quad \cdot \mathbf{n}_{e_{\mathbf{K}}}(\mathbf{x}) \varepsilon^{-i\mathbf{K} \odot \mathbf{x}} d\mathbf{x} \\ &= \int \frac{1}{(2\pi)^N} \left(\int \mathcal{K}_{\Gamma}(\mathbf{x}) \check{g}(\Gamma) \frac{[\mathbf{x}]_{\Gamma}}{[\mathbf{x}]_{\mathbf{K}}} \right. \\ &\quad \left. \times e^{-i(\mathbf{K} \odot \Gamma) \odot \mathbf{x}} d\Gamma \right) d\mathbf{x}, \end{aligned} \quad (\text{A10})$$

where for a probe wave having wave vector \mathbf{K} :

$$\begin{aligned} \mathcal{K}_{\Gamma}(\mathbf{x}) &= \left[\mathbf{n}_{e_{\Gamma}} \left(\frac{1}{\|\mathbf{x} - \mathbf{e}_{\Gamma}\|} - ik \right) \right. \\ &\quad \left. + \mathbf{n}_{r_{\Gamma}} \left(\frac{1}{\|\mathbf{x} - \mathbf{r}_{\Gamma}\|} - ik \right) \right] \cdot \mathbf{n}_{e_{\mathbf{K}}}. \end{aligned} \quad (\text{A11})$$

Then Eq. (A10) can be written as follows:

$$\begin{aligned} \mathcal{F}_{\mathcal{E}}(\mathbf{n}_{e_{\mathbf{K}}} \cdot \nabla g(\mathbf{x})) &= \int \check{g}(\Gamma) \int \check{\mathcal{K}}_{\Gamma}(\mathbf{Z}) \frac{1}{(2\pi)^{2N}} \\ &\quad \times \int \frac{[\mathbf{x}]_{\Gamma} [\mathbf{x}]_{\mathbf{Z}}}{[\mathbf{x}]_{\mathbf{K}}} e^{-i(\mathbf{K} \odot \Gamma \odot \mathbf{Z}) \odot \mathbf{x}} d\mathbf{x} \\ &= \int \check{g}(\Gamma) \int \check{\mathcal{K}}_{\Gamma}(\mathbf{Z}) \delta(\mathbf{K} - \Gamma - \mathbf{Z}) d\mathbf{Z} d\Gamma \\ &= \int \check{g}(\Gamma) \check{\mathcal{K}}_{\Gamma}(\mathbf{K} - \Gamma) d\Gamma. \end{aligned} \quad (\text{A12})$$

With probe-object distances of the order of 1 cm (or more) at usual ultrasonic frequencies (corresponding typically to the standard bandwidth of medical ultrasounds), the terms $1/\|\mathbf{x} - \mathbf{e}_{\Gamma}\|$ and $1/\|\mathbf{x} - \mathbf{r}_{\Gamma}\|$ are small compared with k ; so then

$$\mathcal{K}_{\Gamma}(\mathbf{x}) \simeq -ik[\mathbf{n}_{e_{\Gamma}}(\mathbf{x}) + \mathbf{n}_{r_{\Gamma}}(\mathbf{x})] \cdot \mathbf{n}_{e_{\mathbf{K}}}(\mathbf{x}). \quad (\text{A13})$$

However, as shown in Fig. 13, $\mathcal{K}_{\Gamma}(\mathbf{x})$ varies very slowly with \mathbf{x} , and so the bandwidth of $\check{\mathcal{K}}_{\Gamma}(\mathbf{K})$ is of the order of $c/2R$. It is about 300 times smaller than the central frequency of the transmitted wavelet. Therefore, the angle $(\mathbf{K}, \hat{\Gamma}) < 1^\circ$, and one has

$$\mathcal{K}_{\Gamma}(\mathbf{x}) \simeq \mathcal{K}_{\mathbf{K}}(\mathbf{x}) = -ik[1 + \mathbf{n}_{e_{\mathbf{K}}}(\mathbf{x}) \cdot \mathbf{n}_{r_{\mathbf{K}}}(\mathbf{x})]. \quad (\text{A14})$$

We take “ \otimes ” to denote the (spectral) elliptical convolution defined by

$$\check{g} \otimes \check{\mathcal{K}}_{\mathbf{K}}(\mathbf{K}) = \int \check{g}(\Gamma) \check{\mathcal{K}}_{\mathbf{K}}(\mathbf{K} - \Gamma) d\Gamma. \quad (\text{A15})$$

One obtains the following derivation rule:

$$\mathcal{F}_{\mathcal{E}}(\mathbf{n}_{e_{\mathbf{K}}} \cdot \nabla g)(\mathbf{K}) \simeq \check{g} \otimes \check{\mathcal{K}}_{\mathbf{K}}(\mathbf{K}). \quad (\text{A16})$$

Here, we have extended the classical derivation rule based on plane wave decomposition (using Fourier transforms). In the latter case, the inner integral would reduce to

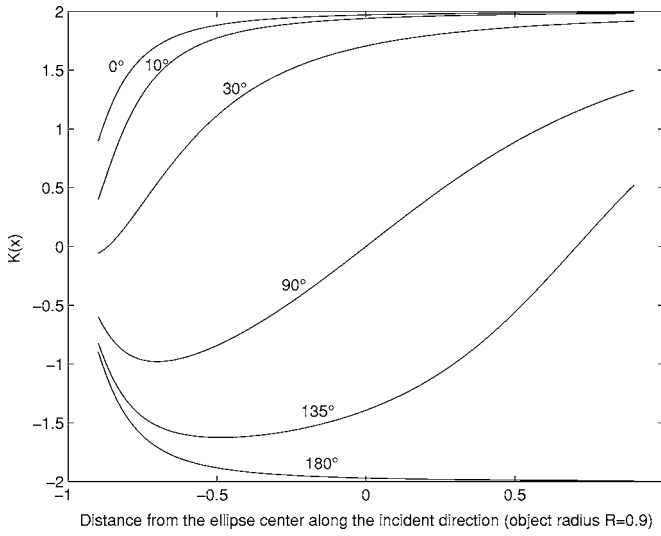


FIG. 13. Profiles of $\mathcal{K}_r(\mathbf{x})$ along the direction \mathbf{n}_ϕ at various angles (\mathbf{K}, Γ).

the distribution $-i2\mathbf{n}_\infty \cdot \mathbf{K} \delta(\mathbf{K} - \Gamma)$ giving the result $\mathcal{F}_\mathcal{E}(\mathbf{n}_\infty \cdot \nabla g)(\mathbf{K}) \approx 2F(\mathbf{n}_\infty \cdot \nabla g)(\mathbf{K}) = -i2\mathbf{n}_\infty \cdot \mathbf{K} F(g)(\mathbf{K})$; the transmitter-receiver being located at infinity. The factor 2 results from the fact that the wave performs a round-trip between the transmitter and the object. As regards the elliptical Fourier transform, the “derivation vector” $\mathcal{K}(\mathbf{x}) = \mathbf{n}_e / \|\mathbf{x} - \mathbf{e}\| + \mathbf{n}_r / \|\mathbf{x} - \mathbf{r}\| - ik(\mathbf{n}_e + \mathbf{n}_r)$ takes into account the curvature of the elliptical wave front.

In addition, if one operates in

$$\text{reflection } \mathbf{n}_{e\mathbf{K}} = \mathbf{n}_{r\mathbf{K}}, \quad \check{\mathcal{K}}_{\mathbf{K}} = -2ik\delta(\mathbf{K}),$$

$$\text{transmission } \mathbf{n}_{e\mathbf{K}} \approx -\mathbf{n}_{r\mathbf{K}}, \quad \check{\mathcal{K}}_{\mathbf{K}} \approx 0. \quad (\text{A17})$$

APPENDIX B: INVERSION OF THE ELLIPTICAL RADON TRANSFORM

Using the elliptical projection-slice theorem, Eq. (35) can be written:

$$f(\mathbf{x}) = \frac{1}{2} \times \frac{1}{\pi} \int_0^\pi \mathcal{F}_{\mathcal{E}|\phi}^{-1} \times [\text{Abs} \circ F \circ \mathcal{R}_\mathcal{E} \circ f](s = n_\phi \odot \mathbf{x}, \phi) d\phi, \quad (\text{B1})$$

where, for an arbitrary ϕ , $\mathcal{F}_{\mathcal{E}|\phi}^{-1}$ is the inverse elliptical Fourier transform:

$$\begin{aligned} & \mathcal{F}_{\mathcal{E}|\phi}^{-1}(\check{f}(S, \phi)|_{\phi \text{ fixed}})(s, \phi) \\ &= \frac{1}{2\pi} \int \check{f}(S, \phi)|_{\phi \text{ fixed}} e^{iS n_\phi \odot \mathbf{x}} [\mathbf{x}]_\phi dS. \end{aligned}$$

In order to obtain the inverse Radon transform, we take \mathcal{O} to denote the angular integration operator over the incident angle ϕ of any well-behaved function h mapping the cylindrical space $\mathcal{Y} = \{(s, \phi); s \in \mathbb{R}, 0 \leq \phi < \pi\}$:

$$\mathcal{O}[h](\mathbf{x}) = \frac{1}{2} \times \frac{1}{\pi} \int_0^\pi h(s = n_\phi \odot \mathbf{x}, \phi) d\phi \quad (\text{B2})$$

and from (Eq. (B1)):

$$f = \mathcal{O} \circ \mathcal{F}_{\mathcal{E}|\phi}^{-1} \circ \text{Abs} \circ F \circ \mathcal{R}_\mathcal{E} \circ f = \mathcal{O} \circ \mathcal{F}_{\mathcal{E}|\phi}^{-1} \circ \text{Abs} \circ \mathcal{F}_{\mathcal{E}|\phi} \circ f \quad (\text{B3})$$

In addition, one can note that

$$\begin{aligned} & [\mathcal{F}_{\mathcal{E}|\phi}^{-1} \circ \mathcal{F}_{\mathcal{E}|\phi} \circ f](\mathbf{x}) \\ &= \frac{1}{2\pi} \int \check{f}(S, \phi) e^{iS n_\phi \odot \mathbf{x}} [\mathbf{x}]_\phi dS \\ &= \int f(\mathbf{y}) \frac{[\mathbf{x}]_\phi}{[\mathbf{y}]_\phi} \frac{1}{2\pi} \int e^{iS n_\phi \odot (\mathbf{x} \odot \mathbf{y})} dS dy \\ &= \int f(\mathbf{y}) \frac{[\mathbf{x}]_\phi}{[\mathbf{y}]_\phi} \delta_{\mathcal{E}, \phi}(\mathbf{x} - \mathbf{y}) d\mathbf{y} = \pi_{f, \phi}(\mathbf{x}), \quad (\text{B4}) \end{aligned}$$

where $\delta_{\mathcal{E}, \phi}(\mathbf{x})$ delineates the ellipse of foci ($\mathbf{e}_\phi, \mathbf{r}_\phi$) crossing the point \mathbf{x} . Then, $\pi_{f, \phi}(\mathbf{x})$ is the *elliptically* backprojected image of the elliptical projection $p_\phi(s)$. In addition we have

$$\begin{aligned} \pi_{f, \phi}(\mathbf{x}) &= \frac{1}{2\pi} \int \int \check{f}(S, \phi) e^{iS s} [\mathbf{x}]_\phi \delta(s - \mathbf{n}_\phi \odot \mathbf{x}) dS ds \\ &= [\mathbf{x}]_\phi \cdot [F^{-1} \circ \check{f}|_{\phi \text{ fixed}}](\mathbf{n}_\phi \odot \mathbf{x}) = [\mathcal{B}_\phi \circ F^{-1} \\ &\quad \circ \check{f}|_{\phi \text{ fixed}}](\mathbf{x}) \\ &= [\mathcal{B}_\phi \circ p_\phi](\mathbf{x}), \quad (\text{B5}) \end{aligned}$$

where for any function h defined on \mathcal{Y} ,

$$\mathcal{B}_\phi[h(s, \phi)](\mathbf{x}) = [\mathbf{x}]_\phi \cdot h(\mathbf{n}_\phi \odot \mathbf{x}, \phi) \quad (\text{B6})$$

is the ϕ -backprojection²² operator on the ellipse perpendicular to the incident direction ϕ . To summarize, we have obtained the following relations:

$$[\mathcal{F}_{\mathcal{E}|\phi}^{-1} \circ \mathcal{F}_{\mathcal{E}|\phi} \circ f](\mathbf{x}) = \pi_{f, \phi}(\mathbf{x}) \quad (\text{B7})$$

$$\mathcal{F}_{\mathcal{E}|\phi}^{-1} = \mathcal{B}_\phi \circ F^{-1}. \quad (\text{B8})$$

The filtered elliptical projections Π_ϕ defined in Eq. (37) can be written:

$$\Pi_\phi = \mathcal{B}_\phi \circ F^{-1} \circ \text{Abs} \circ F \circ \mathcal{R}_\mathcal{E} \circ f = \mathcal{F}_{\mathcal{E}|\phi}^{-1} \circ \text{Abs} \circ \mathcal{F}_{\mathcal{E}|\phi} \circ f. \quad (\text{B9})$$

We retrieve the object function, Eq. (42):

$$\begin{aligned} f &= \mathcal{O} \circ \mathcal{F}_{\mathcal{E}|\phi}^{-1} \circ \text{Abs} \circ F \circ \mathcal{R}_\mathcal{E} \circ f \\ &= \mathcal{O} \circ \mathcal{B}_\phi \circ F^{-1} \circ \text{Abs} \circ F \circ \mathcal{R}_\mathcal{E} \circ f \\ &= \mathcal{B} \circ F^{-1} \circ \text{Abs} \circ F \circ \mathcal{R}_\mathcal{E} \circ f. \quad (\text{B10}) \end{aligned}$$

Finally, the inverse elliptical Radon transform is defined by

$$\mathcal{R}_\mathcal{E}^{-1} = \mathcal{B} \circ F^{-1} \circ \text{Abs} \circ F. \quad (\text{B11})$$

¹S. J. Norton, “Reconstruction of a two-dimensional reflecting medium over a circular domain: Exact solution,” J. Acoust. Soc. Am. **67**, 1266–

- 1273 (1980).
- ²S. J. Norton and M. Linzer, "Ultrasonic reflectivity imaging in three dimensions: Exact inverse scattering solutions for plane, cylindrical and circular apertures," *IEEE Trans. Biomed. Eng.* **28**, 202–220 (1980).
- ³A. J. Devaney, "Generalized projection-slice theorem for fan beam diffraction tomography," *Ultrason. Imaging* **7**, 264–275 (1988).
- ⁴T. J. Cavicchi and W. D. O'Brien, "Numerical study of higher-order diffraction tomography via the sinc basis moment method," *Ultrason. Imaging* **11**, 42–74 (1989).
- ⁵P. Gan, R. Ludwig, and P. L. Levin, "Nonlinear diffractive inverse scattering for multiple scattering in inhomogeneous acoustic background media," *J. Acoust. Soc. Am.* **97**, 764–776 (1995).
- ⁶T. D. Mast, A. I. Nachman, and R. C. Waag, "Focusing and imaging using eigenfunctions of the scattering operator," *J. Acoust. Soc. Am.* **102**, 715–725 (1997).
- ⁷M. P. André, H. S. Jarrée, G. P. Otto, P. J. Martin, and J. P. Jones, "Reduction of phase aberration in a diffraction tomography system for breast imaging," *Acoust. Imaging* **22**, 151–157 (1996).
- ⁸J. W. Wisikin, D. Borup, and S. A. Johnson, "Inverse scattering from arbitrary two-dimensional objects in stratified environments via a Green's operator," *J. Acoust. Soc. Am.* **102**, 853–864 (1997).
- ⁹S. Pourjavid and O. Tretiak, "Ultrasound imaging through time-domain diffraction tomography," *IEEE Trans. Ultrason. Ferroelectr. Freq. Control* **38**, 74–85 (1991).
- ¹⁰C. Q. Lan and W. Xiong, "An iterative method of ultrasonic reflection-mode tomography," *IEEE Trans. Med. Imaging* **13**, 419–425 (1994).
- ¹¹T. D. Mast, "Wideband quantitative ultrasonic imaging by time-domain diffraction tomography," *J. Acoust. Soc. Am.* **106**, 3061–3071 (1999).
- ¹²M. H. Xu and L. H. Wang, "Time-domain reconstruction for thermoacoustic tomography in a spherical geometry," *IEEE Trans. Med. Imaging* **21**, 814–822 (2002).
- ¹³M. H. Xu, Y. Xu, and L. H. Wang, "Time-domain reconstruction and numerical simulations for thermoacoustic tomography in various geometries," *IEEE Trans. Med. Imaging* **50**, 1086–1099 (2003).
- ¹⁴G. Ambartsoumian and P. Kuchment, "On the injectivity of the circular Radon transform," *Inverse Probl.* **21**, 473–485 (2005).
- ¹⁵J. F. Greenleaf, S. A. Johnson, W. F. Wamoya, and F. A. Duck, "Algebraic reconstruction of spatial distributions of acoustics velocities in tissue from their time-of-flight profiles," in *Acoustical Holography* (Plenum, New York, 1975), pp. 71–90.
- ¹⁶S. J. Norton, "Generation of separate density and compressibility images in tissue," *Ultrason. Imaging* **5**, 240–252 (1983).
- ¹⁷A. J. Devaney, "Variable density acoustics tomography," *J. Acoust. Soc. Am.* **78**, 120–130 (1985).
- ¹⁸S. Mensah and J.-P. Lefebvre, "Enhanced compressibility tomography," *IEEE Trans. Ultrason. Ferroelectr. Freq. Control* **44**, 1245–1252 (1997).
- ¹⁹J. P. Jones, "Impediography, a new technique for diagnostic medicine," *Ultrasound in Medicine*, edited by D. N. White (Plenum, New York, 1975), Vol. **1**, pp. 489–497.
- ²⁰S. J. Leeman, "Impediography equation," *Acoustical Imaging*, edited by A. F. Metherell (Plenum, New York, 1980), Vol. **8**, pp. 517–525.
- ²¹J.-P. Lefebvre, "A linearised inverse problem: Acoustic impedance tomography in biological media," in *Electromagnetic and Acoustic Scattering: Detection and Inverse Problem*, edited by C. Bourelly *et al.* (World Scientific, Singapore, 1988), pp. 287–301.
- ²²S. R. Deans, *The Radon Transform and Some of its Applications* (Wiley, New York, 1983), pp. 131–136.
- ²³C. Tsogka, "Modélisation mathématique et numérique de la propagation des ondes élastiques tridimensionnelles dans des matériaux fissurés," ("Numerical and mathematical modeling of elastic wave propagation in fractured materials"), Ph.D. thesis, Université Paris Dauphine—Paris IX, 1999.
- ²⁴E. Bécache, P. Joly, and C. Tsogka, "An analysis of new mixed finite elements for the approximation of wave propagation problems," *SIAM (Soc. Ind. Appl. Math.) J. Numer. Anal.* **37**, 1053–1084 (2000).
- ²⁵F. Collino and C. Tsogka, "Application of the pml absorbing layer model to the linear elastodynamic problem in anisotropic heterogeneous media," *Geophysics* **66**, 294–305 (2001).
- ²⁶R. Waag and R. Fedewa, "A ring transducer system for medical ultrasound research," *IEEE Trans. Ultrason. Ferroelectr. Freq. Control* **53**, 1707–1718 (2006).